Large enhancement of the spin Hall effect in Mn metal by Sn doping

D. Qu, T. Higo, T. Nishikawa, K. Matsumoto, K. Kondou, D. Nishio-Hamane, R. Ishii, P. K. Muduli, Y. Otani, and S. Nakatsuji

Phys. Rev. Materials **2**, 102001 — Published 3 October 2018

DOI: 10.1103/PhysRevMaterials.2.102001

Large enhancement of the spin Hall effect in Mn metal by Sn doping

D. Qu[1], T. Higo[1, 2], T. Nishikawa[1], K. Matsumoto[1], K. Kondou[3], D. Nishio-Hamane[1], R. Ishii[1], P. K. Muduli[1], Y. Otani[1, 2, 3] and S. Nakatsuji[1, 2]

[1]Institute for Solid State Physics, University of Tokyo, Kashiwa 277-8581, Japan

[2]CREST, Japan Science and Technology Agency, Kawaguchi, Saitama 332-0012, Japan

[3]Center for Emergent Matter Science, RIKEN, Wako, Saitama 351-0198, Japan

Abstract:

The recent discovery of the large anomalous Hall effect (AHE) in the non-collinear Kagome antiferromagnets Mn_3X (X=Sn, Ge) has highlighted the compounds and alloys based on the combination of Mn and X. As the spin Hall effect (SHE), and AHE share the same origin, the injection of pure spin current into the alloys based on Mn and X could potentially engender large SHE. Here we report that our spin Seebeck and the spin pumping measurements both reveal that doping Mn with 18% Sn strikingly increases the spin Hall angle of the *amorphous/nanocrystalline* Mn-Sn alloy by as large as 20 times while the resistivity is reduced by 10 times compared with pure Mn. Our study not only serves as essential reference for pure spin current phenomena in Mn-based alloys but may also offer a promising method for exploring future energy saving spin Hall materials.

The study of spin current and its related phenomena has attracted broad attention in the last decades. In particular, pure spin current contains only spin angular momentum but no net charge flow, and thus is expected to be beneficial for low power consumption spintronic device [1]. The spin Hall effect (SHE) converts charge current to transverse spin current due to spin-orbit-coupling [2]. Inversely, spin current can be converted to transverse charge current by the inverse spin Hall effect (ISHE), which provides an essential electrical approach to detect the pure spin current [3, 4].

While the extensive studies have established the SHE in transition heavy metals, magnets have been relatively less explored in terms of SHE as they are time reversal odd. Nonetheless, several pioneer researches have been performed for ferromagnetic metals such as Py and Co [5, 6]. In addition, antiferromagnets have recently attracted much attention as the next generation active element for spintronic devices due to exceptional advantages such as high frequency magnetization dynamics, negligible stray field, and insensitivity to perturbation [7-12]. Among these materials, the non-collinear Kagome lattice antiferromagnets Mn_3X (X=Sn, Ge, Ga) have stood out prominently because of their large transverse responses to static and dynamic electric / magnetic fields. These antiferromagnets have been found to show large anomalous Hall (AHE) [13-16], Nernst effects (ANE) [17, 18] and magnetic optical Kerr effect [19] despite their negligible magnetization. Moreover, the antiferromagnet Mn_3Sn has been experimentally identified as the Weyl magnets for the first

time in magnets [20]. The Weyl points near the Fermi energy serve as sources and drains of the large fictitious field or Berry curvature in the momentum space, which causes the large AHE and ANE [13-18].

These discoveries have highlighted the compounds and alloys based on the combination of Mn and *X* in general. Since SHE/ISHE and AHE share the same origin, it is of great interest to explore spin-charge conversion in Mn-*X* alloys [21]. In addition, since many intriguing magnetic materials are known in the Mn-based compounds, it is essential to study the ISHE in the elemental Mn alone before investigating the interplay between the spin current and the magnetic configuration and the doping effects of *X* elements. In this article, we report ISHE of both Mn and Mn-Sn amorphous/nanocrystalline thin films.

To study the ISHE in the elemental Mn and the Mn-Sn alloys, we employ the thermally generated pure spin current from the spin Seebeck effect (SSE) in the commercially obtained polycrystalline ferrimagnetic insulator yttrium iron garnet (YIG) substrate [22]. We also supplement this result with spin pumping (SP) measurement where pure spin current is created through coherently excited spin-wave [4]. These two independent methods allow us to unambiguously determine two key parameters; namely, the spin Hall angle, θ_{SH}, which evaluates the efficiency between charge and spin conversion, and the spin diffusion length, λ_{sd}, which provides the measure of the average distance spin travels before losing its information. By using an insulator for spin injection, we can avoid parasitic effects from

charge carriers such as anisotropic magnetoresistance, anomalous and planar Hall effects, and shunting effect that may complicate the spin current conversion. Moreover, YIG is particularly useful as recent works have demonstrated that SSE using YIG may generate pure spin current reliably [23] and robustly regardless of its crystallinity [24].

Our analyses of the SSE measurements using a series of samples with different thicknesses have yielded a modest θ_{SH} but long λ_{sd} for Mn. In comparison, the same type of analyses and measurements for amorphous/nanocrystalline non-magnetic $Mn_{82}Sn_{18}$ have revealed striking enhancement of θ_{SH} by a factor of 20, while the resistivity (ρ) is reduced by about 10 times. These estimations are also further confirmed by SP measurements. Our results indicate the energy consumption ($\sim\rho/\theta^2_{SH}$) of $Mn_{82}Sn_{18}$as a spin-orbit-torque spintronic device is nearly 4,000 times smaller than that for Mn [25]. Our work not only serves as an essential reference for studying the pure spin current phenomena in Mn-based alloys, but also indicates that the Sn doping provides a promising method in exploring energy efficient spin Hall materials.

The Mn and Mn-Sn alloy thin films are deposited at room temperature by magnetron sputtering onto YIG substrates from commercially obtained Mn target or Mn_3Sn target, respectively. The details of sample fabrication are available in Supplemental Material [26]. The YIG substrates are 0.5 mm in thickness and 10 mm by 3 mm laterally. No thermal treatment is performed. By using both the inductively coupled plasma atomic emission

spectroscopy (ICP-AES) and the energy dispersive spectroscopy on the scanning electron microscope (EDX-SEM), the composition of the Mn-Sn alloy is determined as $Mn_{82}Sn_{18,}$ see Supplemental Material [26]. The stoichiometry difference between target and thin film is often seen in oxides [27] and sometimes seen in metallic films [28].

We first examined the crystalline quality of the films using the grazing angle X-ray diffractometer (XRD) measurement. As shown in Fig. 1(a), polycrystalline YIG (marked in black) and the polycrystalline α-Mn (marked in red) peaks are observed for the 120-nm thick Mn thin film on YIG. In contrast, the $Mn_{82}Sn_{18}$ film exhibits a much broader XRD peak even at 500 nm as shown in Fig. 1 (b). By using the Scherrer Equation, $B(2\theta) = \lambda / (A \cdot \cos\theta)$, where $B(2\theta)$ is the peak full width at half maximum, λ=0.154 nm is the wavelength of the X-ray using the Cu target, we estimate the grain size A to be 2 nm. This broad peak overlaps with the crystalline peaks of α-Mn, β-Sn, and several Mn-Sn alloys, therefore the $Mn_{82}Sn_{18}$ thin film deposited at room temperature could be a mixture of amorphous and nanocrystalline structure of Mn, Sn and Mn-Sn alloys.

We further investigated the surface morphology of the thin films on YIG by atomic force microscope (AFM). Fig. 1(c) and Fig. 1(d) show AFM scan over a 1μm by 1μm area of the as-deposited 30 nm Mn and 10 nm $Mn_{82}Sn_{18}$ on YIG. We found films are notably smooth with mean roughness of 0.07 nm and 0.15 nm for the Mn and $Mn_{82}Sn_{18}$ film, respectively, which is comparable with the mean roughness of 0.15 nm for the bare YIG substrate. The

AFM image of YIG substrate is shown in Supplemental Material [26]. These results indicate high interface qualities. The resistivity of the Mn/YIG and $Mn_{82}Sn_{18}$/YIG samples were measured by the four-terminal method, Fig. 2(a). We find the ρ for Mn and $Mn_{82}Sn_{18}$ are about 3 mΩcm and 0.3 mΩcm, respectively. Films thinner than 30 nm showed higher resistivities caused by increased boundary/surface scattering as shown in the inset of Fig. 2(d) and Fig. 3(b).

Now we discuss the results for the ISHE in both Mn and $Mn_{82}Sn_{18}$ from the spin current generated by the longitudinal SSE in YIG. The schematic picture of the set-up is shown in Fig. 2(b). The sample, with the film side covered with a thin and soft silicone sheet, is sandwiched between two Cu blocks. The top Cu plate is attached to a resistive heater. The bottom Cu block acts as a heat sink. Using the same geometry, the temperature gradient is simultaneously monitored during the measurement by two thermocouples placed on the top and bottom surfaces of another sample with the same dimension. Under a vertical temperature gradient and in-plane magnetic field, SSE generates a pure magnon spin current in YIG. The pure spin current is injected vertically into the attached metallic layer and is converted into charge current by ISHE. The sign of the thermal voltage determines the sign of θ_{SH} [1].

The spin dependent thermal voltages for Mn on YIG with different Mn thicknesses are shown in Fig. 2(c). Thicker film generates smaller voltages because of finite λ_{sd} and

smaller resistance. The higher voltages in the negative saturation field indicates a negative θ_{SH} for Mn opposite to the Pt case. A part of the magnetic field responses, especially the plateau observed in the low magnetic field region ($|B|$ < 200 Oe), is caused by the non-collinear magnetization between surface and bulk YIG [29]. To demonstrate that the induced thermal voltage comes from the ISHE in Mn, we show that for 55-nm thick Mn layer on Si, no sizable ANE is observed.

The obtained ISHE voltage from the SSE spin current injection can be expressed as [30, 31],

$$\Delta V(t) = 2CL\nabla T\rho(t)\theta_{SH}\frac{\lambda_{sd}}{t}\tanh(\frac{t}{2\lambda_{sd}}) \qquad (1)$$

Here, ΔV is the voltage difference between the positive and negative saturation field, L≈8 mm is the distance between the voltage terminals, ∇T ≈6 K/mm is the temperature gradient and t is the thickness of the metal film. $C = \frac{2e}{\hbar}\frac{\gamma\hbar\rho' k_m^3 l_m}{4\pi M\pi^2}\frac{B_1 B_S}{B_2} g_{eff}^{\uparrow\downarrow} k_B$ is the spin current injection coefficient [31], containing the magnetic properties of YIG (saturation magnetization $4\pi M$=140 kA/m, gyromagnetic ratio γ=1.76×10^{11} s^{-1}T^{-1}, magnon diffusion length l_m=70 nm, finite ferromagnetic insulator thickness factor ρ'~1, maximum wave number k_m=2×10^9 m^{-1}, parameters from diffusion equation B_1=0.55, B_s=2.2×10^{-4}, B_2=5.1×10^{-3}, the Planck constant $\hbar$=1.054×10^{-34} J·s, the electron charge e=1.6×10^{-19} C, the Boltzmann constant k_B=1.38×10^{-23} J·K^{-1}) and the spin mixing conductance ($g_{eff}^{\uparrow\downarrow}$) between the metal layer and YIG. By employing the spin mixing conductance ($g_{eff}^{\uparrow\downarrow}$) available in literature $g_{eff}^{\uparrow\downarrow}$(Mn)= (4.5 ±

0.4)×10^{18} m^{-2} [11], we estimated the spin current injection coefficient to be C≈3.5 $Am^{-1}K^{-1}$. According to Eq. 1, we plot $\Delta V/(L\nabla T\rho)$ to estimate the θ_{SH} and λ_{sd} for Mn with different thicknesses as shown in Fig. 2d. Excluding the first point which drops because of possible spin current back flow, we fit our results with Eq.1. From the fitting, we directly obtained θ_{SH} and λ_{sd} to be θ_{SH}(Mn)=- (0.23 ± 0.03) %, λ_{sd}(Mn)= 11.5 ± 0.15 nm. Both θ_{SH} and λ_{sd} agree very well with the previous report for Mn [11]. The consistent results of θ_{SH}(Mn) also indicates l_m =70 nm may be a good estimation for the magnon diffusion length of our polycrystalline YIG. We noted l_m can be up to a few microns for single crystalline YIG [32, 33]. The shorter l_m in our study could be due to the higher magnon scattering rate induced by different crystal orientations in polycrystalline YIG.

Now we show that 18% Sn doping to Mn well enhances θ_{SH} by an order of magnitude. First, we find the spin dependent thermal voltages ΔV are similar for both $Mn_{82}Sn_{18}$ and Mn, but the ρ is one order of magnitude smaller in $Mn_{82}Sn_{18}$, thus $\Delta V/(L\nabla T\rho)$ is one order of magnitude larger in $Mn_{82}Sn_{18}$. A similar magnetic field response to the Mn case confirms that the voltage also originates from the spin current generated in YIG and thus ISHE (Fig. 3(a)). Moreover, a similar thickness dependence in $\Delta V/(L\nabla T\rho)$ is observed (Fig. 3(b)); the 5-nm thin film has smaller voltage due to spin current back flow. Since very similar $g_{eff}^{\uparrow\downarrow}$ has been reported for Mn and FeMn alloy ($g_{eff}^{\uparrow\downarrow}$(Mn) = (4.5±0.4)×$10^{18}$ and $g_{eff}^{\uparrow\downarrow}$(FeMn) = (4.9±0.4)×$10^{18}$) with very different resistivity on

YIG substrate [11], considering the high interface quality for both Mn/YIG and $Mn_{82}Sn_{18}$/YIG films, similar resistivity for $Mn_{82}Sn_{18}$ and FeMn alloy (~300 μΩcm), the robust and consistent YIG surface quality [30], we assume the same $g_{eff}^{\uparrow\downarrow}$($Mn_{82}Sn_{18}$) = $(4.9\pm0.4)\times10^{18}$ m^{-2} for comparison. By employing the same fitting shown in Fig. 3(b), we find $\theta_{SH}(Mn_{82}Sn_{18}) \approx -(4.4\pm0.7)$ % and $\lambda_{sd}(Mn_{82}Sn_{18}) = 3.7 \pm 0.8$ nm. Notably, the θ_{SH} is far more enhanced by 20 times compared with Mn. In fact, the $\theta_{SH}(Mn_{82}Sn_{18})$ could be smaller with a larger $g_{eff}^{\uparrow\downarrow}$($Mn_{82}Sn_{18}$). To our best knowledge, the largest $g_{eff}^{\uparrow\downarrow}$ for thin metals on YIG reported is Pt/YIG with $g_{eff}^{\uparrow\downarrow}$(Pt) = 6.9×10^{18} m^{-2} [34], and if we assume this $g_{eff}^{\uparrow\downarrow}$ for Mn-Sn, we obtain the lower limit for $\theta_{SH}(Mn_{82}Sn_{18}) \approx -3.1$ % which is still 14 times larger than Mn. Nevertheless, we observed an increase in the total spin to charge conversion including the interfacial transport.

To verify this striking enhancement in the θ_{SH}, we further performed SP measurements on the Mn and $Mn_{82}Sn_{18}$ on polycrystalline bulk YIG samples. The samples are put onto an open coplanar waveguide (CPW) patterned on a SiO_2/Si substrate. Radio frequency (RF) electric current of 9 GHz is passed through the CPW by a signal generator which generates an AC-Oersted field applied to YIG (Fig. 4a). In this configuration, an external dc-magnetic field is applied parallel to CPW to cause the SP effect in the polycrystalline YIG, injecting pure spin current into the adjacent metallic layers. The films are connected to Au electrodes with Ag paste in perpendicular direction to CPW to detect the

rectified voltage generated by ISHE.

Fig. 4(b) shows the ISHE voltage obtained for Pt(10)/YIG (blue), Mn(50)/YIG (orange) and $Mn_{82}Sn_{18}$(50)/YIG (green). Both Mn and $Mn_{82}Sn_{18}$ have negative voltages compared with Pt, consistent with their negative θ_{SH}. The higher resonance field and broad multiple peaks observed are most likely from the polycrystalline nature of the YIG substrate, where the latter is caused by the overlapped resonance spectra from different grains [24]. By using the symmetric Lorentzian function [4], we extract the averaged ISHE voltage from the peaks, and we confirm the expected linear increase of the ISHE voltage as a function of the RF power (Fig. 4(c)). To obtain the θ_{SH}, we employ the following equation derived from ref. 34,

$$\theta_{SH}(M) = \theta_{SH}(Pt)\frac{V_{ISHE}(M)}{V_{ISHE}(Pt)}\cdot\frac{\rho(Pt)}{\rho(M)}\cdot\frac{L(Pt)}{L(M)}\frac{\frac{\lambda_{sd}(Pt)}{t(Pt)}\tanh(\frac{t(Pt)}{2\lambda_{sd}(Pt)})}{\frac{\lambda_{sd}(M)}{t(M)}\tanh(\frac{t(M)}{2\lambda_{sd}(M)})}\cdot\frac{g_{\uparrow\downarrow}(Pt)}{g_{\uparrow\downarrow}(M)} \quad (2)$$

where M represents Mn or $Mn_{82}Sn_{18}$. As the bulk character of YIG (0.5 mm thick) does not allow us to determine $g_{eff}^{\uparrow\downarrow}$, we use the same $g_{eff}^{\uparrow\downarrow}(\mathrm{Mn}) = (4.5 \pm 0.4)\times10^{18}$ m^{-2} for the analysis. By further using the reported values in literature such as $\theta_{SH}(\mathrm{Pt}) \approx 10$ % [34] as well as other quantities obtained in our measurement, the large enhancement of the θ_{SH} in the doped Mn is verified, namely, $\theta_{SH}(Mn_{82}Sn_{18}) \approx -(6.2\pm1.6)$ %, $\theta_{SH}(\mathrm{Mn}) \approx -(0.121\pm0.034)$ %, which are consistent with the SSE results.

To understand the origin of the large θ_{SH} for $Mn_{82}Sn_{18}$, and to detect any contribution

from nanocrystalline magnets such as ferromagnetic Mn_2Sn and non-collinear antiferromagnetic Mn_3Sn, we measured the Hall voltage for the alloy samples on YIG and Si at various temperatures down to 50 K, as shown in Figs. 5(a) and 5(b). We choose thinner film (30 nm) on YIG and thicker film (500 nm) on Si to probe both the interfacial and bulk contribution from $Mn_{82}Sn_{18}$/YIG and $Mn_{82}Sn_{18}$. The Hall effect is found mostly linear with the field and does not exhibit any hysteresis around zero field at all the temperature measured, indicating that the large θ_{SH} is not a result of any magnetic order. A very weak non-linear field dependence of the Hall resistivity is found for $Mn_{82}Sn_{18}$/YIG and is attributed to the spin dependent scattering at the interface [35-37].

Given the absence of the intrinsic magnetic contributions, it is reasonable to compare our observation of the enhancement in θ_{SH} with other similar doping induced changes in θ_{SH} [38-42]. In the Cu and Au cases, the doping of heavy metals such as Bi and Ta is reported to increase θ_{SH}, while reducing λ_{sd}, which has been attributed to the extrinsic mechanism, namely, the increased number of centers for skew or side-jump scattering depending on the scaling relation between ρ and spin Hall resistivity (ρ_{SH}). Thus, the observed enhancement in θ_{SH} and the reduction in λ_{sd} by the Sn doping in Mn metal may point to similar extrinsic mechanism. In fact, θ_{SH} for Sn alone should be negligible as Sn has filled *s* and *d* shells. On the other hand, as a heavy metal, Sn may well increase the effective spin-orbit scattering rate, which is the likely origin of the enhancement in θ_{SH} as well as the reduction in λ_{sd}.

Notably, however, in the case of Sn doped Mn, the θ_{SH} is *increased* with *reducing* ρ, distinctly different from the previous reports where θ_{SH} increases with increasing ρ [39-42]. Considering many of the high θ_{SH} materials have high ρ, our approach of doping a more conductive element in highly resistive materials may enhance the θ_{SH} while reducing their ρ. The energy consumption by spin Hall materials is proportional to ρ/θ^2_{SH} [25], which is 4000 times larger for Mn than that for $Mn_{82}Sn_{18}$ due to 20 times larger θ_{SH} and 10 times smaller ρ. The dramatic difference suggests this approach is beneficial for exploring energy saving spintronic materials.

It is also important to point out that although Mn has a modest θ_{SH} compared to many other transition metals, the 18% Sn doped alloy, being amorphous/nanocrystalline and non-magnetic, exhibits a largely enhanced θ_{SH}. This enhancement could also occur in other Mn based alloys doped with another element. Moreover, recent report for Au_xTa_{1-x} films has shown that θ_{SH} changes smoothly with Au concentration while the system varies from polycrystalline to amorphous/nanocrystalline structures [43]. Similarly, the large θ_{SH} is also expected for the Mn-Sn crystalline films. Therefore, in the study of pure spin current injection in the Mn based alloy, one must be careful in separating the intrinsic contribution from the magnetic configuration and the extrinsic contribution by alien atoms.

To summarize, we have performed a comprehensive study on the inverse spin Hall effect in pure Mn metal and $Mn_{82}Sn_{18}$ amorphous/nanocrystalline alloys by using

combination of thermally and coherently excited spin current from YIG through the spin Seebeck and spin pumping effects. We have obtained consistent results from both measurements and estimated the $\theta_{SH} \approx$ -0.23% and -4.4%, and the $\lambda_{sd} \approx$ 11.5 and 3.7 nm for Mn and $Mn_{82}Sn_{18}$, respectively. The large enhancement of θ_{SH} in the Sn doped Mn not only serves as important reference for the study of SHE/ISHE in Mn based alloys including the Weyl antiferromagnet Mn_3Sn, but more importantly, it provides a viable route for enhancing the θ_{SH} with reducing the ρ, which is beneficial for designing energy saving spintronic materials.

Acknowledgements

We would like to thank Dr. Yufan Li, Prof. C. L. Chien, and Dr. Takumi Ohtsuki for discussion and Prof. Mikk Lippmaa for the AFM support. This work is partially supported by CREST(JPMJCR15Q5), Japan Science and Technology Agency, by Grants-in-Aid for Scientific Research (16H02209), and by Grants-in-Aids for Scientific Research on Innovative Areas (15H05882, 15H05883 and 26103002) from the Ministry of Education, Culture, Sports, Science, and Technology of Japan, and Program for Advancing Strategic International Networks to Accelerate the Circulation of Talented Researchers (No. R2604) from the Japanese Society for the Promotion of Science (JSPS). D.Q. was supported by the Japan Society for the Promotion of Science (JSPS) as international research fellow.

* satoru@issp.u-tokyo.ac.jp

References:

1. A. Hoffmann and S. D. Bader, Phys. Rev. Applied **4**, 047001 (2015)
2. M.I. Dyakonov and V.I. Perel, Phys. Lett. A **35**, 459 (1971)
3. A. Azevedo, L. H. Vilela Leão, R. L. Rodriguez-Suarez, A. B. Oliveira, and S. M. Rezende J. App. Phys. **97**, 10C715 (2005)
4. E. Saitoh, M. Ueda, H. Miyajima and G. Tatara, Appl. Phys. Lett. **88**, 182509 (2006)
5. B. F. Miao, S. Y. Huang, D. Qu, and C. L. Chien, Phys. Rev. Lett. **111**, 066602 (2013)
6. Dai Tian, Yufan Li, D. Qu, S. Y. Huang, Xiaofeng Jin, and C. L. Chien, Phys. Rev. B **94**, 020403(R) (2016)
7. T. Jungwirth, X. Marti, P. Wadley and J. Wunderlich, Nat. Nanotech. **11**, 231 (2016)
8. W. Zhang, W. Han, S.-H. Yang, Y. Sun, Y. Zhang, B. Yan and S. S. P. Parkin, Sci. Adv. **2**, e1600759 (2016)
9. J. B. S. Mendes, R. O. Cunha, O. Alves Santos, P. R. T. Ribeiro, F. L. A. Machado, R. L. Rodríguez-Suárez, A. Azevedo, and S. M. Rezende, Phys. Rev. B **89**, 140406(R) (2014)
10. W. Zhang, M. B. Jungfleisch, W. Jiang, J. E. Pearson, A. Hoffmann, F. Freimuth, and Y. Mokrousov, Phys. Rev. Lett. 113, 196602 (2014)
11. C. Du, H. Wang, F. Yang, and P. C. Hammel, Phys. Rev. B **90**, 140407(R) (2014)
12. D. Qu, S. Y. Huang, and C. L. Chien, Phys. Rev. B **92**, 020418 (R) (2015)
13. S. Nakatsuji, N. Kiyohara and T. Higo, Nature **527**, 212 (2015)
14. N. Kiyohara, T. Tomita, and S. Nakatsuji, Phys. Rev. Applied **5**, 064009 (2016)
15. A. K. Nayak, J. E. Fischer, Y. Sun, B. Yan, J. Karel, A. C. Komarek, C. Shekhar, N. Kumar, W. Schnelle, J. Kübler, C. Felser and S. S. P. Parkin, Science Adv. **2**, e1501870 (2016)
16. G.-Y. Guo and T.-C. Wang, Phys. Rev. B **96**, 224415 (2017)
17. M. Ikhlas, T. Tomita, T. Koretsune, M.-T. Suzuki, D. N.-Hamane, R. Arita, Y. Otani and S. Nakatsuji, Nature Phys. **13**, 1085 (2017)
18. X. Li, L. Xu, L. Ding, J. Wang, M. Shen, X. Lu, Z. Zhu, and K. Behnia, Phys. Rev. Lett. **119**, 056601 (2017)
19. T. Higo, H. Man, D. B. Gopman, L. Wu, T. Koretsune, O. M. J. v. Erve, Y. P. Kabanov, D. Rees, Y. Li, M.-T. Suzuki, S. Patankar, M. Ikhlas, C. L. Chien, R. Arita, R. D. Shull, J. Orenstein and S. Nakatsuji, Nature Photon. **12**, 73 (2018)
20. K. Kuroda, T. Tomita, M.-T. Suzuki, C. Bareille, A. A. Nugroho, P. Goswami, M. Ochi, M. Ikhlas, M. Nakayama, S. Akebi, R. Noguchi, R. Ishii, N. Inami, K. Ono, H. Kumigashira, A. Varykhalov, T. Muro, T. Koretsune, R. Arita, S. Shin, T. Kondo and S. Nakatsuji, Nature Mater. **16**, 1090 (2017)
21. Y. Zhang, Y. Sun, H. Yang, J. Železný, S. P. P. Parkin, C. Felser, and B. Yan, Phys. Rev. B **95**, 075128 (2017)
22. K. Uchida, H. Adachi, T. Ota, H. Nakayama, S. Maekawa, and E. Saitoh, Appl. Phys. Lett.

97, 172505 (2010)
23. D. Qu, S. Y. Huang, Jun Hu, Ruqian Wu, and C. L. Chien, Phys. Rev. Lett. 110, 067206 (2013)
24. F.-J. Chang, J. G. Lin, and S.-Y. Huang, Phys. Rev. Mater. **1**, 031401 (R) (2017)
25. J. Han, A. Richardella, S. A. Siddiqui, J. Finley, N. Samarth, and L. Liu, Phys. Rev. Lett. **119**, 077702 (2017)
26. See Supplemental Material at [URL will be inserted by publisher] for details of the sample fabrication and characterization.
27. T. I. Selinder, G. Larsson, U. Helmersson, P. Olsson, J.-E. Sundgren, and S. Rudner, Appl. Phys. Lett. **52**, 1907 (1988)
28. S. Wurmehl, J. T Kohlhepp, H. J M Swagten, B. Koopmans, C. G F Blum, V. Ksenofontov, H. Schneider, G. Jakob, D. Ebke and G. Reiss, J. Phys. D: Appl. Phys. **42** 084017 (2009)
29. P.-H. Wu and S.-Y. Huang, Phys. Rev. B **94**, 024405 (2016)
30. D. Qu, S. Y. Huang, B. F. Miao, S. X. Huang, and C. L. Chien, Phys. Rev. B **89**, 140407 (R) (2014)
31. S. M. Rezende, R. L. Rodríguez-Suárez, R. O. Cunha, A. R. Rodrigues, F. L. A. Machado, G. A. Fonseca Guerra, J. C. Lopez Ortiz, and A. Azevedo, Phys. Rev. B **89**, 014416 (2014)
32. Andreas Kehlberger, Ulrike Ritzmann, Denise Hinzke, Er-Jia Guo, Joel Cramer, Gerhard Jakob, Mehmet C. Onbasli, Dong Hun Kim, Caroline A. Ross, Matthias B. Jungfleisch, Burkard Hillebrands, Ulrich Nowak, and Mathias Kläui. Phys. Rev. Lett. **115**, 096602 (2015)
33. L. J. Cornelissen, J. Liu, R. A. Duine, J. Ben Youssef and B. J. van Wees, Nature Phys. **11**, 1022 (2015)
34. H. L. Wang, C. H. Du, Y. Pu, R. Adur, P. C. Hammel, and F. Y. Yang, Phys. Rev. Lett. **112**, 197201 (2014)
35. S. Y. Huang, X. Fan, D. Qu, Y. P. Chen, W. G. Wang, J. Wu, T. Y. Chen, J. Q. Xiao, and C. L. Chien, Phys. Rev. Lett. **109**, 107204 (2012)
36. C. Tang, P. Sellappan, Y. Liu, Y. Xu, J. E. Garay, and J. Shi, Phys. Rev. B **94**, 140403(R) (2016)
37. S. S.-L. Zhang and G. Vignale, Phys. Rev. Lett. 116, 136601 (2016)
38.M. Gradhand, D. V. Fedorov, P. Zahn, and I. Mertig, Phys. Rev. B **81**, 245109 (2010)
39. Y. Niimi, M. Morota, D. H. Wei, C. Deranlot, M. Basletic, A. Hamzic, A. Fert, and Y. Otani, Phys. Rev. Lett. **106**, 126601 (2011)
40. A. Fert and P. M. Levy, Phys. Rev. Lett. **106**, 157208 (2011)
41. Y. Niimi, Y. Kawanishi, D. H. Wei, C. Deranlot, H. X. Yang, M. Chshiev, T. Valet, A. Fert, and Y. Otani, Phys. Rev. Lett. **109**, 156602 (2012)
42. P. Laczkowski, Y. Fu, H. Yang, J.-C. Rojas-Sánchez, P. Noel, V. T. Pham, G. Zahnd, C.

Deranlot, S. Collin, C. Bouard, P. Warin, V. Maurel, M. Chshiev, A. Marty, J.-P. Attané, A. Fert, H. Jaffrès, L. Vila, and J.-M. George, Phys. Rev. B **96**, 140405(R) (2017)
43. D. Qu, S. Y. Huang, G. Y. Guo, and C. L. Chien, Phys. Rev. B **97**, 024402 (2018)

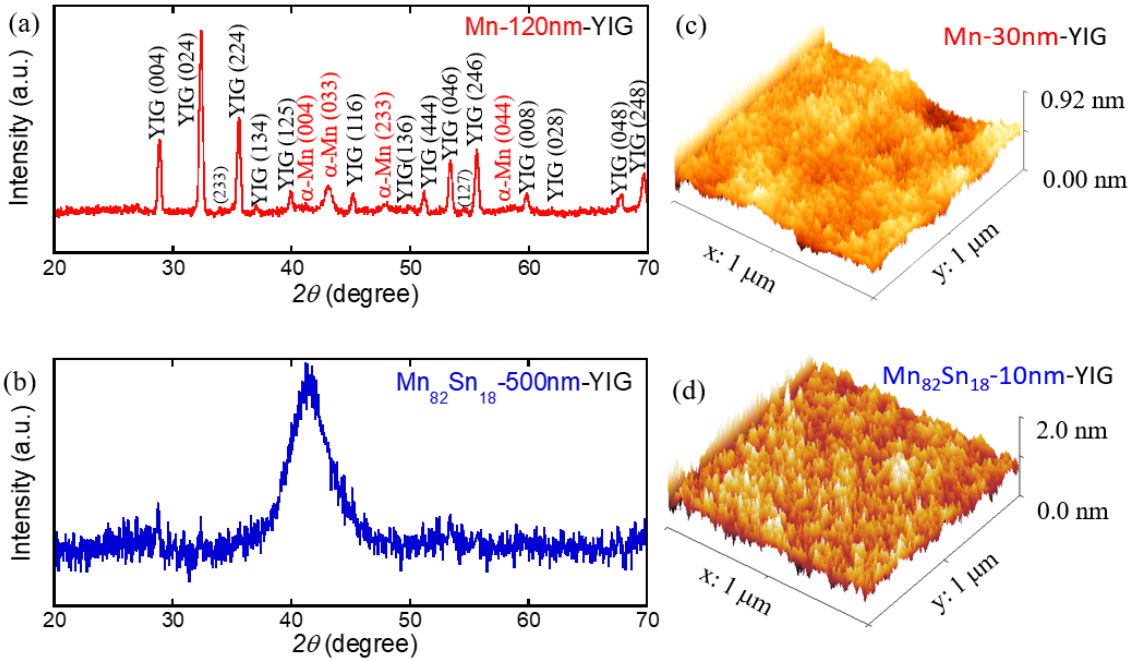

Fig. 1 (color online) Grazing angle XRD pattern for (a) Mn (120 nm)/YIG and (b) $Mn_{82}Sn_{18}$ (500 nm)/YIG. Surface topography probed by AFM for (c) Mn (30 nm)/YIG and (d) $Mn_{82}Sn_{18}$ (10 nm)/YIG, over an area of 1 μm by 1 μm.

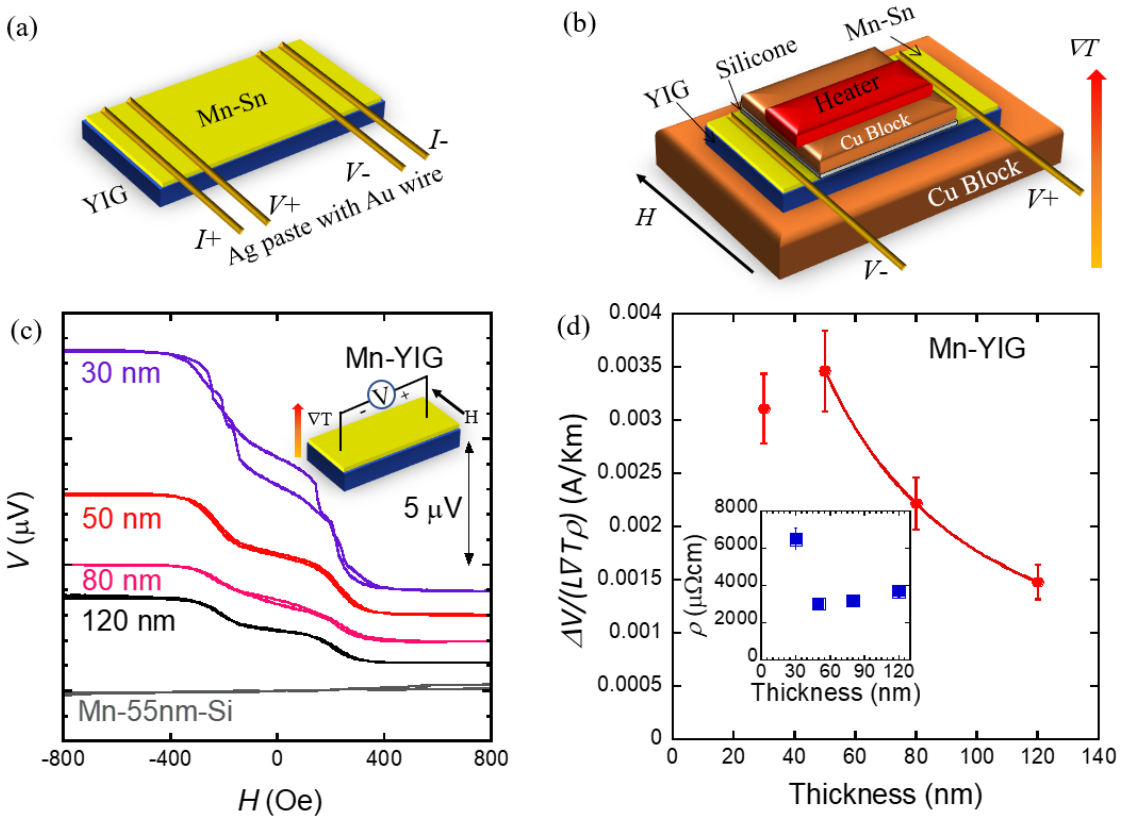

Fig. 2 (color online) Schematic illustration of (a) the four-terminal electric and (b) the thermal transport set-up. (c) Magnetic field dependence of the ISHE voltage for Mn (*t*)/YIG and Mn (55 nm)/Si with various thickness *t*. Inset show schematic measurement geometry. (d) Plot of $\Delta V/(L\nabla T\rho)$ vs. thicknesses for Mn (*t*)/YIG. Solid line is fitting to Eq. 1. Inset is thickness dependent resistivity.

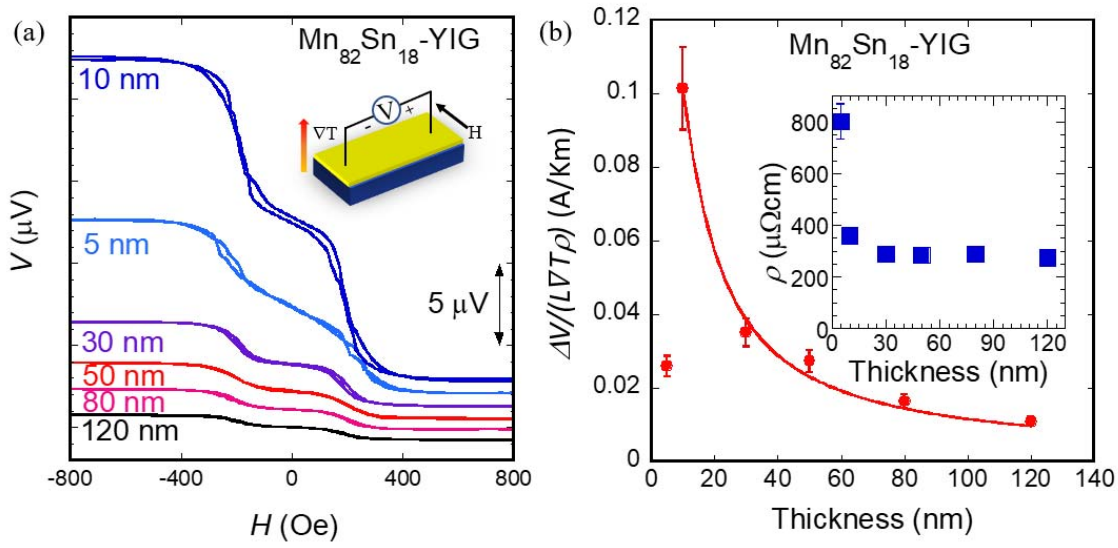

Fig. 3 (color online) (a)Thickness and magnetic field dependence of the ISHE voltage for $Mn_{82}Sn_{18}$ (*t*)/YIG. Inset shows schematic measurement geometry. (b) Plot of $\Delta V/(L\nabla T\rho)$ vs. thicknesses for $Mn_{82}Sn_{18}$ (*t*)/YIG. Solid line is fitting to Eq. 1. Inset is thickness dependent resistivity.

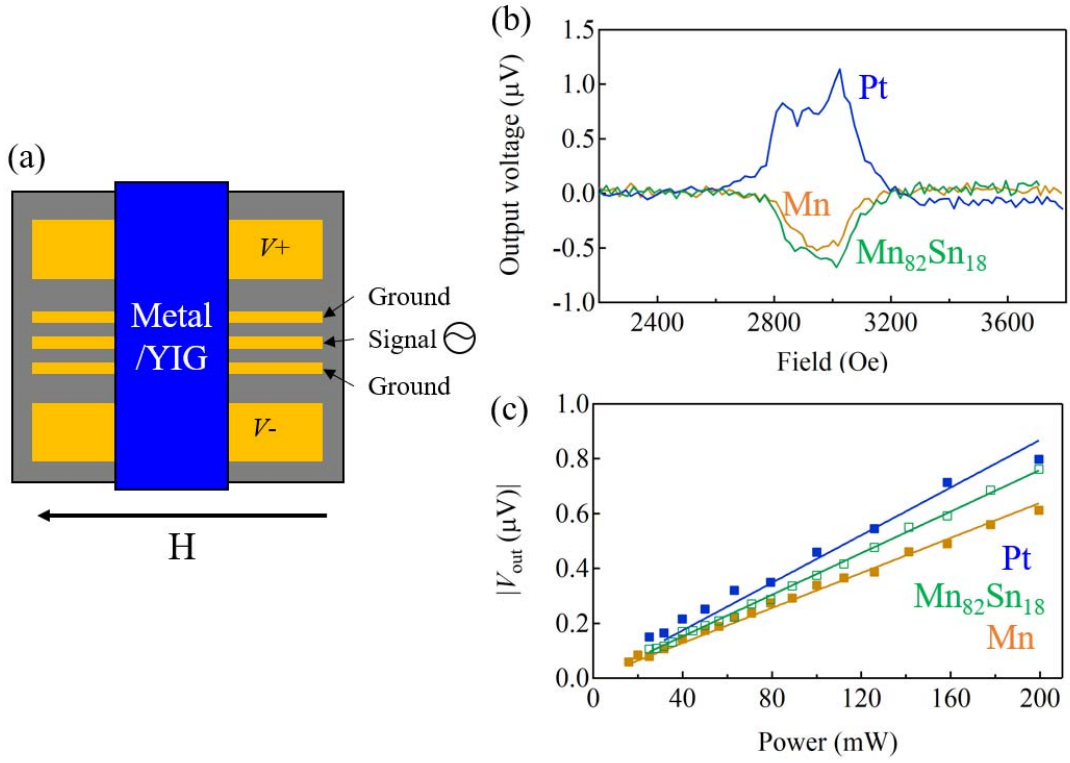

Fig. 4 (color online) (a)Schematic drawing of the CPW. (b) ISHE voltage for Pt (10)/YIG (blue), Mn (50)/YIG (orange) and $Mn_{82}Sn_{18}$/YIG (green). (c) RF power dependence of the ISHE voltage

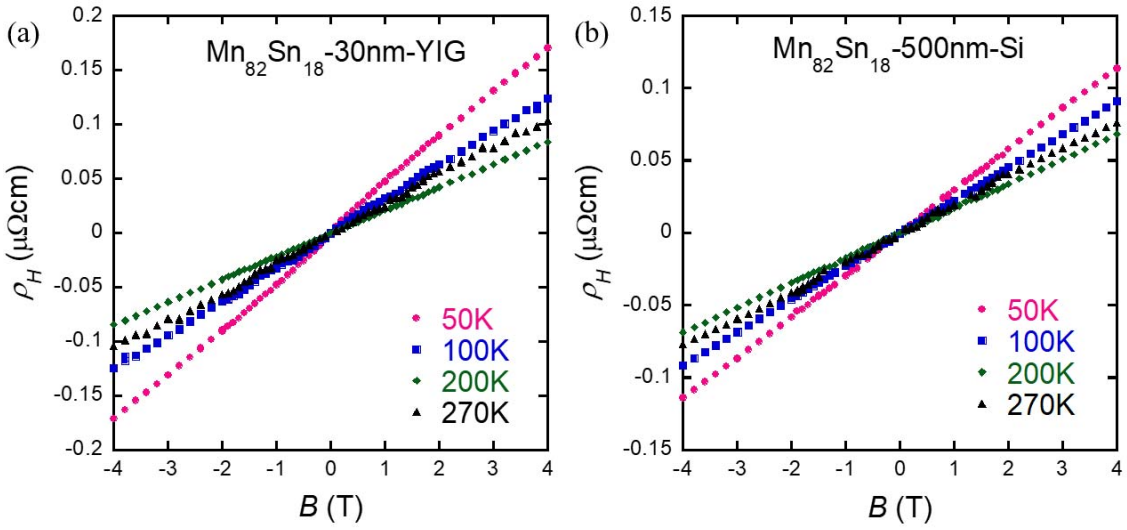

Fig. 5 (Color online) Magnetic field dependence of the Hall resistivity for (a) $Mn_{82}Sn_{18}$ (30 nm)/YIG and (b) $Mn_{82}Sn_{18}$ (500 nm)/Si obtained at various temperatures.